Surface roughness of asteroid (162173) Ryugu and comet 67P/Churyumov-Gerasimenko inferred from in-situ observations

K. A. Otto,[1]⋆ K.-D. Matz,[1] S. E. Schröder,[1] R. Parekh,[1] K. Krohn,[1] R. Honda,[2] S. Kameda,[3]
R. Jaumann,[1,4] N. Schmitz,[1] K. Stephan,[1] S. Sugita,[5,6] E. Tatsumi,[5,7] T.-M. Ho,[8] A. Koncz,[1]
F. Trauthan,[1] Y. Cho,[5] M. Hayakawa,[9] C. Honda,[10] T. Kouyama,[11] M. Matsuoka,[9] T. Morota,[5]
S. Mottola,[1] K. Ogawa,[9] F. Preusker,[1] N. Sakatani,[3] H. Sawada,[9] F. Scholten,[1] H. Suzuki,[12]
M. Yamada,[6] Y. Yokota,[8] K. Yoshioka[13]

[1]*German Aerospace Center, Institute of Planetary Research, Rutherfordstraße 2, 12489 Berlin, Germany*
[2]*Kochi University, Department of Information Science, 2-5-1 Akebono, Kochi, Japan*
[3]*Rikkyo University, Department of Physics, 3-34-1 Nishi-Ikebukuro, Toshima, Tokyo, Japan*
[4]*Free University of Berlin, Institute of Geosciences, Malteserstraße 74-100, 12249 Berlin, Germany*
[5]*University of Tokyo, Department of Earth and Planetary Science, 7-3-1 Hongo, Bunkyo, Tokyo, Japan*
[6]*Planetary Exploration Research Center, Chiba Institute of Technology, 2-17-1 Tsudanuma, Narashino, Chiba, Japan*
[7]*University of La Laguna, Instituto de Astrofísica de Canrias, Calle Vía Láctea, s/n, 38205 San Cristóbal de La Laguna, Santa Cruz de Tenerife, Spain*
[8]*German Aerospace Center, Institute of Space Systems, Robert-Hooke-Str. 7, 28359 Bremen, Germany*
[9]*Japan Aerospace Exploration Agency, Institute of Space and Astronautical Science, 3-3-1 Yoshinodai, Chuo, Sagamihara, Kanagawa, Japan*
[10]*University of Aizu, Aizu Research Center for Space Informatics, Aizu-Wakamatsu, Fukushima, Japan*
[11]*National Institute of Advanced Industrial Science and Technology, 2-3-26 Aomi, Koto, Tokyo, Japan*
[12]*Meiji University, Department of Physics, 1-1-1 Higashimita, Tama, Kawasaki, Kanagawa, Japan*
[13]*University of Tokyo, Department of Complexity Science and Engineering, 5-1-5 Kashiwanoha, Kashiwa, Chiba, Japan*

ABSTRACT

Alteration processes on asteroid and comet surfaces, such as thermal fracturing, (micrometeorite) impacts or volatile outgassing, are complex mechanisms that form diverse surface morphologies and roughness on various scales. These mechanisms and their interaction may differ on the surfaces of different bodies. Asteroid Ryugu and comet 67P/Churyumov-Gerasimenko, both, have been visited by landers which imaged the surfaces in high spatial resolution. We investigate the surface morphology and roughness of Ryugu and 67P/Churyumov-Gerasimenko based on high resolution in situ images of 0.2 mm and 0.8 mm pixel resolution over an approximately 25 cm and 80 cm wide scene, respectively. To maintain comparability and reproducibility, we introduce a method to extract surface roughness descriptors (fractal dimension, Hurst exponent, joint roughness coefficient, root mean square slope, hemispherical crater density, small scale roughness parameter and Hapke mean slope angle) from in situ planetary images illuminated by LEDs. We validate our method and choose adequate parameters for an analysis of the roughness of the surfaces. We also derive the roughness descriptors from 3-dimensional shape models of Ryugu and orbiter camera images and show that the higher spatially resolved images results in a higher roughness. We find that 67P/Churyumov-Gerasimenko is up to 6% rougher than Ryugu depending on the descriptor used and attribute this difference to the different intrinsic properties of the materials imaged and the erosive processes altering them. On 67P/Churyumov-Gerasimenko sublimation appears to be the main cause for roughness, while on Ryugu micrometeoroid bombardment as well as thermal fatigue and solar weathering may play a significant role in shaping the surface.

Key words: planets and satellites: fundamental parameters – comets: general – minor planets, asteroids: general – methods: data analysis – techniques: image processing

1 INTRODUCTION

The roughness of airless planetary surfaces is an influential parameter for remote sensing observations of celestial bodies. It has important impact on the photometric behaviour of a surface and therefore influ-

ences measurements of reflectance spectroscopy including imagery (Hapke 1984) and thermal emission (Davidsson et al. 2015).

Methods to derive the surface roughness from a planetary body have been developed for various scales. On large scales, roughness is an important parameter for the geologic interpretation of planetary terrains (Helfenstein 1988; Steinbrügge et al. 2020). It also causes effects such as self-heating when light is reflected and radiated to

⋆ E-mail: katharina.otto@dlr.de

another point on a planetary surface due to the local tilt of the terrain. This can increase local erosion or activity on comets and the Yarkovsky and YORP-effects on asteroids (Keller et al. 2015; Rozitis & Green 2013, 2012). These effects are usually accounted for with a sufficiently high resolution shape models which have been derived for many planetary missions from image data (Preusker et al. 2019, 2015) or laser altimetry (Barnouin-Jha et al. 2008). The latter allows the derivation of surface roughness from the pulse width of the reflected laser beam (Steinbrügge et al. 2018).

On smaller scales, surface roughness influences the spectral rock signature at wavelengths from the visible to thermal spectrum (Davidsson & Rickman 2014; Hapke 1981). Generally it is assumed that planetary surfaces are covered with a particulate medium that depending on the particle size and shape influences the reflectance spectra of the observed surface (Hiroi & Peters 1991). However, with increasing spatial resolution of the spectral data the porosity and roughness of the surface material can influence the spectral contrast, spectral shape and the absolute reflectance/emission due to additional volume scattering and cavity effects (Rost et al. 2018) and should be taken into account in order to avoid a misinterpretation. In addition, the roughness on scales that cause shadowing effects or small scale self-heating have to be considered when interpreting near-infrared and thermal measurements (Davidsson et al. 2009). However, only topographic features larger than the thermal skin depth, usually in the centimetre scale, affect these measurements (Davidsson et al. 2015). For example, the thermal skin depth of asteroid Ryugu is approximately 1.5–3 cm (Hamm 2019) and 0.6 cm for comet Churyumov-Gerasimenko (Davidsson et al. 2016).

The Hayabusa2 sample collection procedure revealed that boulders on C-type asteroid Ryugu are covered with a layer of fine grained particles (<1 mm) that were removed from the boulder surfaces during the collection process (Morota et al. 2020). In situ observations of Ryugu as well as comet Churyumov-Gerasimenko reveal that their surfaces are depleted in fine grained materials and that the majority of surface features are bare rocks or centimetre to decimetre sized particle assemblies (Jaumann et al. 2019; Mottola et al. 2015; Schröder et al. 2017a; Yano et al. 2006). The rock surface roughness has implications for the shear strength and friction angles of the regolith with higher surface roughness introducing higher friction between the constituents (Jiang et al. 2006; Reeves 1985; Xu & Sun 2005).

In applied geological sciences the roughness is often estimated by visually comparing a rock profile with a standard roughness scale (Barton & Choubey 1977). More objective methods involve determining the fractal dimension or the root mean square of the slope distribution (RMS-slope) of rock profiles (Lee et al. 1997; Tse & Cruden 1979). The RMS-slope is also commonly used as roughness parameter in thermal modelling (Davidsson et al. 2015; Rozitis & Green 2013). Another roughness parameter taking into account more complex surface structures, including overhangs and caves, is the small scale roughness parameter, which is the geometric measure of the surface area in relation to its flat projected area (Davidsson & Rickman 2014; Lagerros 1997).

In this work we will extract roughness parameters from the only two surfaces of small bodies imaged in situ: asteroid Ryugu and comet Churyumov-Gerasimenko. This allows us to derive the millimeter scale roughness measured over a horizontal scale of a few tens of centimetres of the two volatile-rich bodies, compare them quantitatively and discuss the different alteration processes' influence on the surface structure. To gain insight of the dependence of roughness on the spatial scale, we also apply our method to two global images from Ryugu and Churyumov-Gerasimenko. By doing so we avoid any influence that the method of derivation may have on the result."

In the following sections we first summarize the space mission operation at Ryugu and 67P and their main observations (Section 2), followed by a detailed description of the data used in this work (Section 3). In Section 4 we introduce the roughness parameters and methods developed to extract them. Section 5 includes an analysis of the model parameters and summarizes the roughness parameters of Ryugu and 67P. Section 6 discusses the influence of the model parameters and possible formation mechanisms of surface roughness. Finally, a discussion of the wider context of the results and its conclusion is given in Sections 7 and 8, respectively.

2 IN SITU OBSERVATIONS

Before deriving roughness parameters for Ryugu and Churyumov-Gerasimenko, we first introduce the general scene of the landing sites.

2.1 Scene of the MASCOT landing site

In June 2018 JAXA's Hayabusa2 mission rendezvoused with Cb-type near-Earth asteroid Ryugu (Watanabe et al. 2019, 2017). Ryugu is a top-shaped asteroid of approximately 950 m diameter (Figure 1a). Its relatively low density of $1.19 \, g/cm^3$ suggests a high bulk porosity (>50%) and rubble pile structure (Watanabe et al. 2019). Ryugu is relatively dark with a geometric albedo of 4.0% at 0.55 µm (Tatsumi et al. 2020; Sugita et al. 2019) and has been linked to CI or CM meteorites (Jaumann et al. 2019; Kitazato et al. 2019; Sugita et al. 2019). The surface and regolith appear rough, covered with rocks and boulders of various sizes and shapes (Sugita et al. 2019) while smaller particles in the sub-centimetre size range and dust are missing (Jaumann et al. 2019). Four morphologic types of boulders have been identified (Sugita et al. 2019): the unique bluish boulder Otohime Saxum near the south pole, bright and mottled, bright and smooth, and dark and rugged boulders. The last two types have also been observed by the Mobile Asteroid Surface Scout (MASCOT) during its descent and the rugged boulder type has additionally been observed in situ in high image resolution on Ryugu's surface (Figure 1c).

MASCOT was detached from the Hayabusa2 spacecraft on 3rd October 2018 and after the initial descent phase and relocation on the surface, MASCOT landed near a crumbly and rough boulder which it observed in situ with four on-board instruments (Jaumann et al. 2019) (camera, radiometer, magnetometer and spectrometer (unable to return expected data) (Ho et al. 2017)) including a high resolution camera (MasCam) (Jaumann et al. 2017). Due to a slight tilt towards the surface (22° with respect to the surface plane), a field-of-view of 55° and the Scheimpflug optics of MasCam, resolutions down to 0.15 mm could be achieved in the lower part of the images while at the same time maintaining image sharpness for larger distances. Additionally, MasCam was equipped with an LED array composed of four individual colours (blue, green, red, NIR) for illumination during night time. A mini-move by MASCOT allowed observing of the scene from two different directions, which was used to derive a three dimensional shape model of the observed rough boulder on a spatial scale down to ~3 mm (Figure 2a) (Scholten et al. 2019).

MasCam showed a scene, approximately 25 cm across, highlighting a bare boulder with bright inclusions in the millimetre scale, but visible absence of sand and pebble-sized particles (Jaumann et al. 2019). This in combination with the radiometric measurements led to the conclusion that the boulder is highly porous (28%–55%) and that the tensile strength is relative low (200–280 kPa) (Grott et al. 2019). In fact, small pores larger than 1 mm could not be observed while
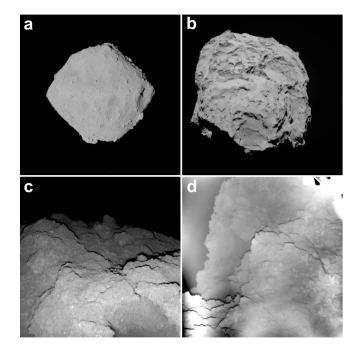
Figure 1. Asteroid Ryugu and comet 67P/Churyumov-Gerasimenko imaged from orbit (upper row) and in situ (lower row). a) Ryugu is approximately 900 m in diameter. b) Churyumov-Gerasimenko from a frontal view with the small lobe in front of the big lobe (~2.5 km across). c) In situ image of Ryugu illuminated with MasCam's red LED. The scene is approximately 25 cm across. The darker appearing area in the lower right corner is a cave (~7 cm wide). d) In situ image at Philae's second landing site on Churyumov-Gerasimenko illuminated with ROLIS' red LED. The scene is approximately 80 cm across. Stray light is clearly visible as alternating light and dark circular areas originating from the lower edge of the image. The overexposed feature in the top right is caused by Philae's leg.
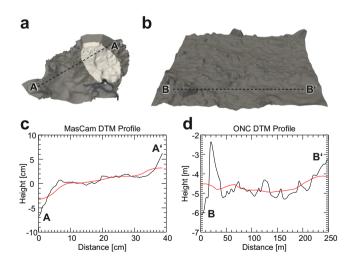

Figure 2. The 3-dimensional shape models used in this work and representative profiles. a) The MasCam shape model from the in situ observation of Ryugu. The scene is approximately 25 cm across and a facet is about 3 mm wide. The light shaded area is the MARA footprint. b) ONC DTM of the area around Mascot's landing site (50 m × 50 m at 20 cm spatial resolution). c)-d) Profiles through MasCam and ONC DTM (black lines) as indicated in a) and b), respectively. The red line is the reference surface.

smaller pores may be present but not resolvable within the Mas-Cam image (Grott et al. 2019). The three dimensional scene shows a prominent hollow in the foreground with a size of approximately 7 cm with multiple smaller indentations (~2 cm) and a roughly 2 cm extended overhang at the right hand corner of the scene (Figure 1c). The hollow and indentations have a convex shape. Cauliflower-like undulations on the scale of ~1 cm form the surface texture of the boulder. They are covered with further, smaller undulations of approximately 2–3 mm, which suggests a fractalnature of the surface. Although there are exceptions, the feature size of 1 cm and 2–3 mm appears to be characteristic for this scene.

The images of MasCam show a cauliflower-like rock surface texture, which can also be observed for cohesive fine grained materials. This is particularly evident in the images acquired during night when the LEDs were used to illuminate the surface. This structural appearance resembles pristine cometary material observed in situ by the Philae lander comet Churyumov-Gerasimenko (Bibring et al. 2015; Schröder et al. 2017a) and is also similar to fracture surfaces of aqueously altered carbonaceous chondrites (Fuchs et al. 1973; Gounelle & Zolensky 2014). We will discuss the similarities and differences between Ryugu's and Churyumov-Gerasimenko's surface texture in more detail in this work.

2.2 Scene of the ROLIS landing site

On November 12th the Philae lander on board the Rosetta mission was detached and landed on comet Churyumov-Gerasimenko (Ulamec et al. 2016). After the initial touchdown and bounce, Philae got to rest at the Abydos site, a relatively rough terrain on the comet. Churyumov-Gerasimenko is a bi-lobate Jupiter family comet with dimensions 4.3 km × 2.6 km × 2.1 km (Jorda et al. 2016). With an estimated bulk porosity of 70–75% (Jorda et al. 2016), Churyumov-Gerasimenko is more porous than asteroid Ryugu. Churyumov-Gerasimenko is relatively dark with a geometric albedo of 6.2% at 0.55 μm (Ciarniello et al. 2016). Geomorphologically, Churyumov-Gerasimenko possesses a north-south dichotomy exhibiting a rough consolidated terrain in the south and a smooth airfall-covered terrain in the north. This is probably caused by the increased erosion of the southern hemisphere during the perihelion passage (Keller et al. 2015). The rough terrain of the southern hemisphere, where Philae came to its final rest, is composed of consolidated material of 10–50 cm thickness (Knapmeyer et al. 2018). This layer probably formed by sintering and cementing of volatiles and dust in the near surface layers (Spohn et al. 2015). Two camera systems on-board Philae, CIVA and ROLIS, showed this consolidated rough terrain in detail (Poulet et al. 2016; Schröder et al. 2017a). Similarly to MasCam on Ryugu (Jaumann et al. 2019), CIVA reports on two types of textures within the field of view - a smooth fine-grained and a rough granular texture (Poulet et al. 2016). ROLIS describes a consolidated jagged surface with cracked plates. Schröder et al. (2017a) also note the fractal nature of Churyumov-Gerasimenko's surface by describing similar surface morphologies on various scales.

The ROLIS camera on-board Philae operated in a similar manner to MasCam on Ryugu. Both cameras possess a 1024 m × 1024 m sensor and a four colour LED array (465–812 nm (MasCam), 470–870 nm (ROLIS)) for illuminating the near surface (Jaumann et al. 2017; Mottola et al. 2007). ROLIS was mounted underneath the Philae lander and was focussing on a surface 30 cm away from the lens. At this distance the field of view of 58° has a pixel resolution of 0.33 mm (Mottola et al. 2007). However, as Philae landed on its side and thus ROLIS partly pointed to the horizon ROLIS' infinity lens, aimed to be employed for long distances during descent, yielded the

best image of the scene on Churyumov-Gerasimenko (Schröder et al. 2017a).

ROLIS showed an approximately 80 cm × 80 cm scene at Philae's second landing site on comet Churyumov-Gerasimenko (Figure 1d). Similarly to Ryugu, no individual grains or pebbles were detected on the surface, but some ejected particles were visible moving along the horizon (Schröder et al. 2017a). A bimodal brightness distribution with dark smooth patches and bright areas running along rough edges are visible. The albedo variation has been suggested to be the result of different degrees of consolidation of the same material with the light areas being less consolidated compared to the dark areas. The surface also appears to have no visible inclusions or pores above ~1 mm in size (Schröder et al. 2017a). The surface morphology of Churyumov-Gerasimenko appears similar to Ryugu with cauliflower-like patterns and undulations, but of slightly larger extent of ~5 cm. The cometary structure seems somewhat more ragged, illustrated by small ~1 cm slots and pointy ridges.

3 DATA

3.1 MASCOT on Ryugu

We used in situ images acquired by MasCam at the second landing site at 22°S and 317°E (Jaumann et al. 2019). At this location the main science cycle was conducted and day and night time images were taken. For the evaluation of roughness, we chose the image acquired during night time illuminated with the red LED (image tag: F1087378791_701_29464_r2, exposure time: 3 ms, image depth: 14 bit) as the stray light in this image appears the least prominent (Schröder et al. 2020) and the contrast highest compared to the other illumination colours (Figure 1c). This image is 1024 × 1024 pixels large and has a pixel resolution of approximately 0.2 mm across the foreground of the image which is the focus of our analysis. A geometric correction of the image was not applied as the effects are negligible.

A shape model of the scene observed by MASCOT and a 50 m × 50 m large shape model with a spatial resolution of 20 cm and 124000 facets derived from Hayabusa2's optical navigation cameras (ONC) images of MASCOT's landing site (Preusker et al. 2019; Scholten et al. 2019) were used to independently derive the RMS-slope and small scale roughness parameter for comparison with our method (Figure 2).

3.2 Philae on 67P/Churyumov-Gerasimenko

We analyse the roughness of a cometary rock using images taken on Churyumov-Gerasimenko by the ROLIS camera on-board the Philae lander on Rosetta (Mottola et al. 2007). However, the ROLIS images are highly affected by stray light introduced by the lens system and an overexposed part of the lander foot in one corner of the image. Thus we used the enhanced and processed red image published by Schröder et al. (2017a) for our analysis (Figure 1d). The image is slightly out of focus, however, as we will see below (Section 4.2) this will not affect our conclusions. The pixel resolution of this image is approximately 0.8 mm in the foreground with a total of 1024 × 1024 pixels.

3.3 Global Analysis

Finally, we used two global images acquired with the red filters of the orbiter cameras on-board Hayabusa2 (ONC-T (Kameda et al. 2017))

and Rosetta (OSIRIS (Keller et al. 2007)) to extract large scale roughness values with our method (Figure 1a-b). The image of Ryugu (image tag: hyb2_onc_20180925_091520_twf_l2d) has an image depth of 10 bit and a size of 1024 x 1024 pixels. For validating the quality of our method we also used the blue version of this image which was taken a minute after the red image and is visually almost identical to the red image (image tag: hyb2_onc_20180925_091624_tbf_l2d). The image of Churyumov-Gerasimenko (image tag: NAC_2014-08-06T01.20.01.282Z_ID30_1397549600_F28) has an image depth of 14 bit and is with 2028 × 2048 pixels twice as large as the other images used in this work. Both images have a spatial resolution of approximately 2 m. Here, we chose an image showing a frontal view of Churyumov-Gerasimenko to avoid the bi-lobate shape of the comet to influence our results. Both global images are geometrically corrected to minimize large scale distortion effects on the analysis.

4 METHOD

In this work we report on the topographic surface roughness on asteroid Ryugu and comet Churyumov-Gerasimenko from space mission images. We introduce a new objective and reproducible method to extract eight commonly used roughness parameters including the RMS-slope, hemispherical crater density, fractal dimension, Hurst exponent, JRC, small scale roughness parameter and Hapke mean slope angle from such images. Before describing the method (Sections 4.2 and 4.3), we first introduce the roughness parameters in detail (Section 4.1).

4.1 Description of roughness parameters

4.1.1 RMS-slope

The RMS-slope distribution of a planetary surface can be derived when the topography of a body is known. Given a local or global shape model composed of N connected facets, the RMS-slope s is defined as the root of the square of each facet's slope θ_i weighted by the projection of the facet area a_i onto the local reference plane (Davidsson et al. 2015; Rozitis & Green 2011; Spencer 1990):

$$s = \sqrt{\frac{\sum_{i=1}^{N} \theta_i^2 a_i \cos \theta_i}{\sum_{i=1}^{N} a_i \cos \theta_i}} \tag{1}$$

In order to assess spatially unresolved roughness of remote sensing data from space missions, specifically those of thermal infrared emission observations, various roughness models have been established (Davidsson et al. 2015). A commonly used model assumes that the unresolved roughness can be represented by a flat surface speckled with spherical-section craters (Buhl et al. 1968; Spencer 1990). The parameters defining the roughness are the crater density f and the ratio between crater depth and crater curvature diameter $\delta = \frac{1}{2}(1 - \cos \gamma)$, where γ is the largest slope angle of the crater. The RMS-slope is then defined as (Davidsson et al. 2015; Lagerros 1996):

$$s = \sqrt{\frac{f}{2}\left(\gamma^2 - \frac{(\gamma \cos \gamma - \sin \gamma)^2}{\sin \gamma^2}\right)} \tag{2}$$

The RMS-slope in this model depends on two parameters f and γ, however in many cases of modelling roughness on airless bodies, hemispherical craters are assumed ($\gamma = 90°$, $\delta = 0.5$) so that the

RMS-slope simplifies:

$$s_{\delta=0.5} = \sqrt{\frac{f}{2}\left(\frac{\pi}{4}-1\right)} \qquad (3)$$

A saturation of hemispherical craters results in a RMS-slope of $49°$. This model has also been applied by Grott et al. (2019) when calculating the thermal conductivity of the boulder observed on Ryugu from thermal infrared measurements. A hemispherical crater density of $f = 0.34$ represents a good agreement with their measurement. On Churyumov-Gerasimenko the hemispherical crater density is highly dependent on the geologic setting and varies between 0.1 and 0.8 (Marshall et al. 2018). For comparability, we will also use the hemispherical crater density in this work.

4.1.2 Small scale roughness parameter

The small scale roughness parameter ξ describes the ratio between the area of a rough surface a_r and its projection onto a reference surface a_p (Davidsson et al. 2009; Davidsson & Rickman 2014):

$$\xi = 1 - \frac{a_p}{a_r} \qquad (4)$$

The advantage of this parameter is that it considers the contribution of cavities and overhangs of a rough surface which cannot be represented by the RMS-slope. It approaches 1 for very rough surfaces. For some thermal roughness models, including the crater roughness model described above, the small scale roughness parameter is identical to the small scale self-heating parameter when scattering is neglected (Davidsson & Rickman 2014; Lagerros 1998, 1997). Using a thermophysical model reproducing temperatures extracted from the near-infrared spectrum of comet 9P/Tempel 1, Davidsson et al. (2009) found that small scale self-heating parameter values between 0.6 and 0.75 are common for the comet and values as low as 0.2 were also found in smoother areas.

4.1.3 Hapke mean slope angle

Another popular roughness parameter, commonly used in spectral investigations of remote sensing data, is the Hapke mean slope angle $\bar{\theta}$ of a rough surface. Hapke (1984) assumes that the roughness is introduced by flat facets with normally distributed orientations and defines the Hapke mean slope angle of these facets as

$$\tan\bar{\theta} = \frac{2}{\pi}\int_0^{\pi/2}\tan\theta\, a(\theta)d\theta \qquad (5)$$

where a is a normalized Gaussian distribution of not too large slope angles θ. Following Lagerros (1997), the relationship between Hapke's mean slope angle and the small scale roughness parameter ξ (Equation 4) can be expressed as

$$\xi = 1 - \frac{E_1(\cot^2\bar{\theta}/\pi)}{\pi\tan\bar{\theta}\,\mathrm{erfc}(\cot\bar{\theta}/\sqrt{\pi})} \qquad (6)$$

if the slopes follow a Gaussian distribution. Here, $E_1(x) = \int_1^\infty \exp(-xt)/t\, dt$. In the roughness regime of most planetary surfaces ($\bar{\theta} \approx 20° - 40°$), the relationship between ξ and $\bar{\theta}$ is nearly linear with a slope of 0.009 $1/°$ (Figure 3).

As we will see later, the criterion that the slope distribution is normally distributed is a consequence of the method we will apply and this assumption is therefore valid. However, the constraint to small angles will pose some difficulties as we will discuss in Section 7.
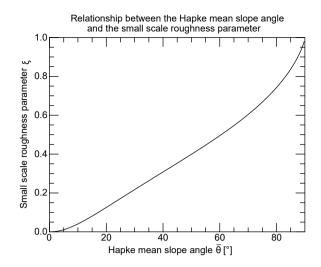

Figure 3. Relationship between the Hapke mean slope angle and small scale roughness parameter (Equation 6). The relationship is approximately linear in the regime of most planetary surfaces with $\xi \approx 0.009 \cdot \bar{\theta}$.

4.1.4 Fractal dimension, Hurst exponent and joint roughness coefficient

The fractal dimension is a measure of the surface roughness of self-affine structures (Zahouani et al. 1998). Fractal surfaces possess the characteristic that with decreasing measuring unit r the total length of the measured surface L increases monotonically (Huang et al. 1992; Mandelbrot 1967):

$$L(r) = r^{D-1} \qquad (7)$$

where D is the fractal dimension, which varies between 1 for smooth and 2 for rough 2-dimensional surfaces. Fractal descriptions have been found to be useful in various geologic applications including the description of coastlines and the joint surfaces of rocks (Mandelbrot 1967; Odling 1994).

The fractal dimension is dependent on the dimension of the space, e.g. 2 or 3-dimensional, it has been determined for. The Hurst exponent H is linearly related to the fractal dimension, independent of the dimension of space and varies between 0 and 1 for smooth and rough contours/surfaces, respectively (Shepard & Campbell 1998):

$$H = 2 - D \qquad \text{(for 2-dimensional profiles)} \qquad (8a)$$
$$H = 3 - D \qquad \text{(for 3-dimensional surfaces)} \qquad (8b)$$

A way to construct such a fractal surface is the Koch curve. Starting with a straight line segment, a triangle with base length l and height h is placed in the centre of the line forming the first order Koch curve. The repetition of this procedure on each of the first order line segments generates the second order and so on, creating a fractal structure. In geoscientific applications, natural rock joints are often assumed to follow a construction similar to the Koch curve (Xie & Pariseau 1994). The advantage is that the fractal dimension can be estimated from a single length scale of a two dimensional contour using the equation

$$D = \frac{\log 4}{\log(2(1 + \cos(\tan^{-1}(2h/l))))} \qquad (9)$$

where h and l are the average height and base length of high-order asperities of a rock joint (Li & Huang 2015; Xie & Pariseau 1994)
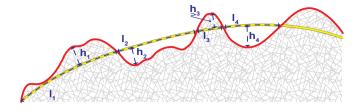
Figure 4. Illustration of the derivation of the fractal dimension of a 2-dimensional profile. Shown is the measurement (blue dashed lines) of base length and asperity height of a natural contour (red line). The reference contour is sketched as yellow line.

(Figure 4). The fractal dimension of the equilateral Koch curve with $h = \sqrt{3/2}l$ yields $D = \log 4/\log 3 = 1.26$.

The fractal dimension can be correlated to the joint roughness coefficient (JRC), a measure of the roughness of rock joints used to estimate the peak shear strength of a material. The JRC has been empirically related to the fractal dimension by the formula (Li & Huang 2015):

$$JRC = 118.89(D - 1)^{0.4343} \qquad (10)$$

The peak shear strength τ of a joint rock surface is given by

$$\tau = \sigma_n \tan\left(JRC \log\left(\frac{JCS}{\sigma_n}\right) + \Phi_b\right) \qquad (11)$$

where σ_n is the effective normal stress, JCS is the joint wall compressive strength and Φ_b is the basic friction angle (Barton 1976). Note that both, τ and σ_n, have the unit of a pressure.

4.2 Roughness from 2-dimensional images

To extract the surface roughness from images acquired in situ on asteroid Ryugu and comet Churyumov-Gerasimenko with the highest available spatial resolution, we derive the RMS-slope, hemispherical crater density, small scale roughness parameter, Hapke mean slope angle, fractal dimension, Hurst exponent and JRC from the outline of imaged rocks applying an objective and reproducible method suitable for images acquired with LED illumination. Due to its high quality and resolution, we tested our method and its dependence on the input parameters using the MasCam image (Section 5.1).

Our method is based on the observation that the texture and material imaged is relatively homogeneous over an area smaller than the rock but large enough to be statistically relevant (>1000 pixels). Within the illuminated images, it can be assumed that parts of the rock with the same distance to the LED have a similar radiance and that with increasing distance the radiance decreases ($\propto r^2$). This makes areas with the same distance from the camera similarly bright in the image. Thus, we aim at determining the 2-dimensional surface at a specific distance, represented by pixels of similar radiance. It can be imagined as a cut through the rock perpendicular to the camera at a specific distance. The texture caused by bright or dark inclusions and varying surface tilts at this specific distance is considered by computing the histogram of pixel brightness values at the given distance and by assuming a Gaussian distribution of these pixel values. The mean and variance of this distribution allow constraining pixels belonging to a specific distance by their brightness values.

More precisely, looking at the in situ images (Figure 5a-b), for each image investigated we identified structures (labelled front left, middle, cave, front right and back right on Ryugu and left edge and
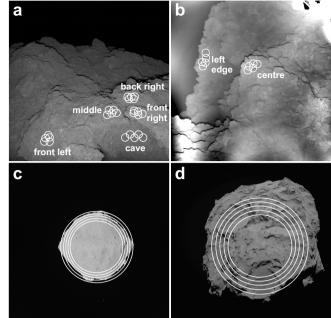

Figure 5. The four images used in this work. Each region to be analysed (labelled in upper row) was investigated using five slightly varying starting regions (white circles). Note that the number of regions investigated in each image varies and that a different starting region selection procedure was applied for the global images. Here, the size of the starting regions varies with the smaller starting regions being a subset of the larger ones, whereas the in situ images have overlapping staring regions of the same size. a) Red MasCam image of Ryugu (~0.2 mm spatial resolution). b) Red ROLIS image of Churyumov-Gerasimenko (~0.8 mm spatial resolution). Note the stray light emerging from the lower image boundary as quasi-circular alternating light and dark regions. The starting regions were chosen in areas which are less dominated by stray light. c) ONC image of Ryugu at ~2 m spatial resolution. d) OSIRIS image of Churyumov-Gerasimenko at ~2 m spatial resolution.

centre on Churyumov-Gerasimenko (Figure 5a-b)) of which to measure the surface roughness. Where available, we also used a shape model to make sure that the structures had a more or less constant distance to the camera. Within these structures we defined five circular starting regions that covered a representative texture and colour of the structure to investigate (Figure 5). The regions comprised ~1835 pixels within the in situ images. Within the MasCam image this corresponds to a roughly 1 cm in diameter circle on the rock surface. For each structure, we derived the roughness parameters by growing all of the five circular starting regions using a standard growing algorithm (see below for details) and averaged the results to generate a representative value.

We also used two global images of Ryugu and Churyumov-Gerasimenko to derive the roughness parameters on a larger scale. For these we used a slightly different approach taking advantage of the fact that the background of the images is black space and therefore easily distinguishable. The five circular starting regions covered the majority of the imaged object (Figure 5c-d). Comprising dark pixels showing space in the circular starting regions, results in a pixel value histogram with two peaks, one at the average asteroid/comet pixel value and one at the average space pixel value, which would allow a precise determination of the object's limb. However, we used circular starting regions that predominantly cover the object to be consistent with the approach used for structures in the in situ images. The five
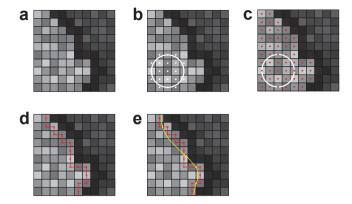
Figure 6. Sketch illustrating the method used in this work. a) Image composed of pixels with lighter area to the left separated from a darker area to the right by a dark shadow. b) Starting region in the light area. The large white circle illustrates the starting region. Pixels with white dots belong to the starting region. c) The grown region marked by red dots. d) Boundary pixels (red dots) and their connection (red lines). e) Boundary contour (red) and reference contour (yellow). The yellow dots illustrate the boundary between adjacent sections as needed for deriving the fractal dimension (compare with Figure 4b).

Figure 7. Illustration of the growing region algorithm in the middle of the MasCam image. a-c) The MasCam image with circular starting region (white), rough detected outline (red) and smoothed reference contour (yellow). b) and c) are subsets of a) as indicated by the white box. Note that the rough outline follows the shadow detected closest to the starting region rather than the most prominent one. d) Histogram of all pixel values within the grown region. The blue histogram represents the histogram of the starting region as shown in e). The dashed and dashed dotted lines indicate the mean and one sigma standard deviation, respectively.

circular starting regions had varying sizes ranging from $0.5\text{-}1.2 \cdot 10^6$ pixels for Churyumov-Gerasimenko and $0.8\text{-}1.4 \cdot 10^5$ for Ryugu. Each smaller circular staring region was a subset of the larger ones.

We then grew each of these regions using a region growing algorithm. Figure 6 and 7 illustrate our method. We determined the mean and standard deviation of the pixels' values within each circular starting region (7e) and added all connected neighbouring pixels (each pixel has eight neighbours) that had radiance values falling within the mean plus/minus a multiple of the standard deviation to the region (Figure 6c and 7e). Pixels not fulfilling this criteria but being surrounded by pixels fulfilling it were also considered part of the grown region. In general we constrained the values using one standard deviation around the mean, but also investigated the effect when changing this range (Section 5.1). The boundary of this grown region was then used as the structure's boundary profile. The boundary pixels are connected in a closed loop (red line in 7a) with each boundary pixel having exactly one preceding and one following neighbour within the eight surrounding pixels (6d).

Although in some cases, specifically the MasCam observations, the image quality appears relatively good the roughness on the pixel scale is not solely introduced by the topography of the rock surface. Instead effects such as image noise, point spreading of particularly bright features and rock texture introduce a roughness to the rock surface that needs to be neglected when deriving the topographic roughness. In order to remove such factors, we applied a morphologic operator to the grown region. By mathematically closing the grown region with a circular structural element (dilation followed by erosion) we filled indentations of the size of the structural element along the contour boundary (e.g. Gonzalez & Woods 2018). This process also counteracts any biases arising from blurry image boundaries.

Inclusions are the most prominent disturbance along the boundary within the rocks on Ryugu. Their size ranges from 0.1 to 2 mm with a characteristic size of 3 pixels in the area investigated. We therefore chose the size of the structural element for the closing operation to be 3 pixels across, but also investigated the influence of different sizes of the structural element.
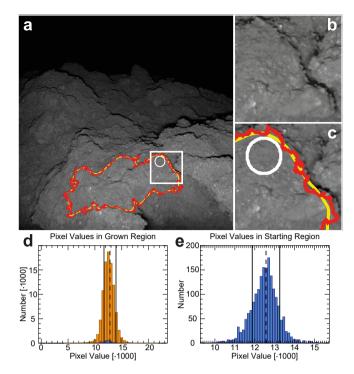
To derive the above described roughness parameters from the boundary, a reference contour is needed. This reference contour represents the assumed local rock topography without any roughness. Although all roughness parameters depend on this reference contour, it is often chosen arbitrarily in the literature. Here, we derived the reference contour by applying a running mean along the rough boundary contour. For each point along the boundary we derived the mean x-y-position including the preceding 50 and following 50 pixels along the boundary. Within the MasCam images, 100 pixels correspond to roughly 2 cm length which is an appropriate length scale given the size of indentations and overhangs described in Section 2.1. This smoothened boundary was used as the reference contour (Figure 6e, 7a and 7c). We also experimented with changing the length of the running mean. Note that the constraint formulated by Hapke (1984), that the slope angles follow a Gaussian distribution (Section 4.1.3), is automatically fulfilled when applying a running mean to define the reference contour.

Given the reference contour and the rough boundary contour of a specific structure identified in the high resolution images, we derived the RMS-slope of the rough contour by determining the angle between the line connecting two adjacent pixels along the rough boundary contour and the line connecting the corresponding pixels on the reference contour. Following Equation 1, we derived the RMS-slope from this angle and the length of the section between the two adjacent pixels on the rough contour. Because the derivation of the RMS-slope requires a 3-dimensional surface boundary rather than a 2-dimensional surface contour, we assumed that the depth of

the pixel along the direction of the boresight vector is the same as the pixel dimension in the image, e.g. 1. This allowed us to simply use the distance between two pixels as the facet area required in Equation 1. Using the angle between the reference and rough boundary contour as described above and again assuming that the extent of the pixels along the boresight vector is 1, we derived the small scale roughness parameter by projecting the rough boundary segment onto the reference contour and applying Equation 4.

Finally, we derived the fractal dimension of the rough boundary contour with respect to the reference contour by finding the intersections of the rough boundary contour and the reference contour. For each section bounded by two adjacent intersections (Figure 6e) we derived the base length by calculating the distance between the two adjacent intersections along the reference contour and the local height by calculating the maximum distance of any rough boundary pixel located in this section to the reference contour (Figure 4b). We then derived the fractal dimension applying Equation 9 by repeating these calculations for each section bounded by two adjacent intersections and determining the average base length and height from all sections. We then applied Equation 10 to estimate the JRC.

4.3 Roughness from 3-dimensional shape models

Additionally, we derived the roughness parameters from two local shape models. For a comparison with the roughness estimated by fitting thermal measurements (Grott et al. 2019), we considered the roughness of the MARA footprint in the MasCam DTM separately. As reference surface we used an arbitrary sphere. Note that the radius of this sphere is not necessary to determine, because the angle between a facet's and the sphere's local normal vectors is independent of the radius of the sphere.

Furthermore, we determined the fractal dimension and corresponding Hurst exponent and JRC for these differently resolved shape models near the MASCOT landing site. These parameters are derived from 2-dimensional contours. Thus, we extracted 10 arbitrary profiles each and calculated the reference contour for the 20 cm resolution ONC DTM by smoothing the profiles consisting of 250 data points (50 m) with a running mean of 100, which corresponds to approximately 20 m, maintaining the same ratio between the DTM spatial resolution and smoothing resolution (0.01) as applied in the image based method described above. Due to the small length of the profiles of the 3 mm resolution MasCam DTM (53 to 121 data points, 16 to 39 cm), the smoothing factor was chosen to be 34 (10 cm), which is on average the same ratio between profile length and smoothing factor as chosen for the ONC DTM, and thus maintains comparability. Profiles crossing through the cave in the front of the MasCam DTM were not considered due to restrictions of our 2.5D profile extraction tool. To derive a representative fractal dimension, Hurst exponent and JRC we averaged the results from the individual profiles. The so derived 2-dimensional fractal dimension is comparable to the 3-dimensional value (Cai et al. 2018; Tatone & Grasselli 2009).

5 APPLICATION AND RESULTS

5.1 Effect of input parameters on roughness

In order to access the reliability of our results and its sensitivity to the chosen parameters, we used the basic parameter set as described in Section 4.2 for the middle region in the MasCam image (smoothing factor of reference contour = 100, standard deviation multiplier = 1,
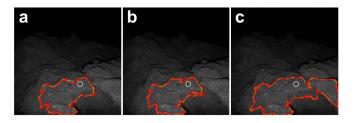

Figure 8. The effect of noise on growing a region in the middle of the image. The white, red and yellow outlines represent the staring region from with the growing algorithm started (compare with Figure 5a), rough contour and reference contour. a) Original image, b) additive noise of 10% of the mean pixel value, c) additive noise of 50% of the mean pixel value. Note that the grown region approaches the image boundary on the right in c) which causes a smaller fractal dimension.

size of structural element = 3, image pixel resolution = 1) and varied one parameter at a time. The result is summarized in Table 1.

To explore the robustness of our method against image noise, we added a Gaussian random noise to the MasCam image with a scale factor of 10% and 50% of the mean pixel value of the image. As shown in Figure 8, the area detected by the grow region algorithm varies slightly in the 10% noise image (Figure 8b) and expands to the right side in the 50% noise image (Figure 8c) compared to the original image (Figure 8a). This can be explained by noisy pixels bridging shadows and allowing the algorithm to grow into areas that are separated by a shadow in the image without or little noise. We then extracted the roughness values and found that the RMS-slope and corresponding hemispherical crater density slightly decrease (for 10% noise level) and increase (for 50% noise level) when introducing noise, but they agree within their errors. The fractal dimension and derived values (Hurst exponent and JRC) show the opposite effect of a very small increase in roughness for a 10% noise level and a decrease for 50% noise level. This decrease can be explained by the growing region reaching the image border to the right and therefore artificially detecting a flat boundary. The small scale roughness parameters and Hapke mean slope angles are constant within their errors. This inconsistency in roughness variation and the low variation within the derived roughness values with additive noise shows that the image noise does not have a systematic effect on the roughness derived. This is achieved by the mathematical closing of the detected boundary, which effectively erases any noise along the boundary on the scale of the structural element.

The filters and camera settings also have an effect on the point spread function on the detector and therefore on the quality of an image. The point spread function is dependent on the incident angle, camera temperature and wavelength. We investigated whether the wavelength influences the result of our method by repeating the global analysis of Ryugu with a blue Ryugu image taken a minute after the red image shown in Figure 5c. Both, the red and blue image, are visually nearly identical and so we used the exact same starting region locations. The roughness derived from the blue and red images are either identical or agree within one sigma standard deviation. We thus conclude that the wavelength the image was taken at and the according point spread function does not have a significant effect on the roughness derived from an image.

The smoothing factor to generate a reference contour was chosen to be 100, e.g. a running mean of 100 points was applied to the boundary surface. Increasing this number results in a smoother and decreasing in a rougher, more similar to the boundary surface, reference contour. The RMS-slope and corresponding hemispheri-

Table 1. Parameters describing the roughness of the rock on Ryugu derived directly from the in situ image for the representative region in the middle of the image. The effect of different input parameters on the derived roughness parameters is shown. The errors are the one sigma standard deviation derived from five locally varying starting regions and, where deduced from other values, derived via standard error propagation.

Input				Result						
Standard deviation multiplier	**Size of structural element**	**Image resolution**	**Smoothing factor reference contour**	**RMS slope [°]**	**Hemispherical crater density**	**Fractal dimension**	**Hurst exponent**	**JRC**	**Small scale roughness parameter**	**Hapke mean slope angle [°]**
1	**3**	**1**	**100**	**36.8 ± 0.4**	**0.56 ± 0.01**	**1.18 ± 0.01**	**0.82 ± 0.01**	**55.9 ± 1.0**	**0.331 ± 0.006**	**42.6 ± 0.8**
↔	↔	↔	↔ 10% noise	36.6 ± 0.9	0.56 ± 0.03	1.18 ± 0.01	0.82 ± 0.01	56.5 ± 1.8	0.330 ± 0.006	42.4 ± 0.8
↔	↔	↔	↔ 50% noise	37.6 ± 0.4	0.59 ± 0.01	1.15 ± 0.01	0.85 ± 0.01	52.4 ± 1.3	0.330 ± 0.004	42.4 ± 0.5
1	3	1	50	36.3 ± 0.3	0.55 ± 0.01	1.16 ± 0.003	0.84 ± 0.003	53.6 ± 0.5	0.322 ± 0.004	41.6 ± 0.5
1	3	1	200	38.1 ± 0.3	0.60 ± 0.02	1.19 ± 0.01	0.81 ± 0.01	58.0 ± 1.2	0.333 ± 0.003	42.8 ± 0.4
1	3	1	300	38.9 ± 0.3	0.63 ± 0.01	1.18 ± 0.01	0.82 ± 0.01	56.4 ± 1.6	0.329 ± 0.008	42.3 ± 1.0
1.5	3	1	100	36.2 ± 0.2	0.54 ± 0.01	1.14 ± 0.02	0.86 ± 0.02	51.2 ± 2.6	0.314 ± 0.003	40.1 ± 0.4
2	3	1	100	36.0 ± 0.2	0.54 ± 0.01	1.14 ± 0.01	0.86 ± 0.01	50.5 ± 1.8	0.304 ± 0.003	39.5 ± 0.4
3	3	1	100	34.6 ± 0.6	0.50 ± 0.01	1.12 ± 0.02	0.88 ± 0.02	46.7 ± 3.2	0.287 ± 0.010	37.6 ± 1.3
1	1 (no erosion)	1	100	37.9 ± 0.1	0.60 ± 0.003	1.28 ± 0.04	0.72 ± 0.04	68.4 ± 4.2	0.343 ± 0.003	43.8 ± 0.4
1	5	1	100	36.8 ± 0.2	0.56 ± 0.01	1.14 ± 0.01	0.86 ± 0.01	51.0 ± 1.1	0.310 ± 0.005	40.2 ± 0.6
1	3	2	100/2 → 50	37.0 ± 0.8	0.57 ± 0.02	1.20 ± 0.02	0.80 ± 0.02	59.5 ± 2.0	0.333 ± 0.015	42.8 ± 1.9
1	3	2	100	37.3 ± 0.6	0.58 ± 0.02	1.21 ± 0.04	0.79 ± 0.04	59.6 ± 4.5	0.328 ± 0.011	42.2 ± 1.4
1	3	4	100/4 → 25	36.6 ± 0.7	0.56 ± 0.02	1.22 ± 0.01	0.78 ± 0.01	61.1 ± 1.2	0.328 ± 0.013	42.2 ± 1.7
1	3	4	100	37.4 ± 0.6	0.58 ± 0.02	1.29 ± 0.04	0.71 ± 0.04	69.0 ± 4.7	0.340 ± 0.008	43.6 ± 1.0
1	3	8	100/8 → 12.5	35.4 ± 1.7	0.52 ± 0.05	1.18 ± 0.06	0.82 ± 0.06	55.3 ± 8.7	0.292 ± 0.034	38.2 ± 4.4
1	3	16	100/16 → 6.25	32.0 ± 3.3	0.43 ± 0.09	1.12 ± 0.04	0.88 ± 0.04	46.8 ± 8.3	0.239 ± 0.025	32.4 ± 3.4

Table 2. Parameters describing the roughness of Ryugu derived from different datasets. The asterisk (*) indicates an average contour derived by smoothing with a running mean of 100, a standard deviation multiplier for the region growing method set to 1 and a consideration of all neighbours. Outline indentations in the order of the bright inclusion size (3 pixels across) where removed from the high resolution images. The errors are the one sigma standard deviation derived from five locally varying starting regions and, where deduced from other values, derived via standard error propagation. The outline of the global image was not smoothed.

Dataset	Method	RMS slope [°]	Hemispherical crater density	Fractal dimension	Hurst exponent	JRC	Small scale roughness parameter	Hapke mean slope angle [°]
ONC shape model of 50 m × 50 m around MASCOT landing site, spatial resolution of ∼20 cm (124000 facets)	Spencer 1990, from profiles	26.7	0.3	1.008 ± 0.003	0.992 ± 0.003	14.1 ± 2.7	0.128	20.3
MasCam shape model, spatial resolution of ∼3 mm (14111 facets)	Spencer 1990, from profiles	34.9	0.51	1.011 ± 0.006	0.989 ± 0.006	16.4 ± 3.8	0.321	41.4
MasCam shape model of MARA's footprint with spatial resolution of ∼3 mm (4711 facets)	Spencer 1990	26.2	0.28				0.141	21.7
MARA 8-12 µm filter daytime measurement	Thermal fitting	28.6	0.34					
MasCam image back right	this work*	35.4 ± 0.3	0.52 ± 0.01	1.11 ± 0.01	0.89 ± 0.01	46.3 ± 2.2	0.279 ± 0.003	36.8 ± 0.4
MasCam image cave	this work*	38.1 ± 0.9	0.60 ± 0.03	1.19 ± 0.02	0.81 ± 0.02	57.4 ± 2.7	0.342 ± 0.010	43.7 ± 1.3
MasCam image front right	this work*	34.9 ± 1.4	0.51 ± 0.04	1.11 ± 0.01	0.89 ± 0.01	45.6 ± 1.8	0.293 ± 0.015	38.3 ± 2.0
MasCam image front left	this work*	37.6 ± 0.3	0.59 ± 0.01	1.20 ± 0.04	0.80 ± 0.04	58.7 ± 4.4	0.330 ± 0.007	42.4 ± 0.9
MasCam image middle	this work*	36.8 ± 0.4	0.56 ± 0.01	1.18 ± 0.01	0.82 ± 0.01	55.9 ± 1.0	0.331 ± 0.006	42.6 ± 0.8
MasCam image mean	this work*	36.6 ± 1.4	0.56 ± 0.04	1.16 ± 0.04	0.84 ± 0.04	52.8 ± 6.3	0.315 ± 0.027	40.8 ± 3.5
ONC global image (red)	this work*	32.9 ± 2.2	0.45 ± 0.06	1.08 ± 0.02	0.92 ± 0.02	38.8 ± 4.0	0.263 ± 0.038	35.0 ± 5.1
ONC global image (blue)	this work*	32.0 ± 1.5	0.43 ± 0.04	1.08 ± 0.03	0.92 ± 0.03	39.4 ± 6.1	0.251 ± 0.022	33.7 ± 3.0

cal crater density increase steadily with increasing smoothing factor. This behaviour is expected, because the reference contour's similarity to the boundary contour decreases with increasing smoothing factor and therefore results in a higher roughness. A similar trend is observed for the small scale roughness parameter and Hapke mean slope angle with an exception for the highest smoothing factor of 300, which is the lowest value. However, the error on this value is comparatively large and points at an outlier within the individual starting regions' results. The fractal dimension and derived parameters (Hurst exponent and JRC) show no obvious trend with increasing smoothing factor. The more similar the reference contour is to the boundary contour (e.g. the smaller the smoothing factor), the more intersections of the reference and boundary contour exist and the more values for the average section length and height can be taken into consideration generating a larger statistic, but not necessarily different values. Thus, a smoothing factor of 100 is reasonable for the scene observed.

The standard deviation multiplier is used to define the cut-off value for the growing region. All pixels with values lying within the mean plus/minus the standard deviation times its multiplier of the starting region are considered for growing the region. Changing the standard deviation multiplier results in different cut-off values with larger regions for larger multipliers. All roughness values show a decrease in roughness with increasing standard deviation multiplier. The larger the standard deviation multiplier, the larger are the grown regions and the distances to the camera they cover. Particularly at a large distance from the camera, the brightness gradient is smaller and borders of the grown region are smoother, which is represented in the lower roughness values. Also, boundaries that align with the image frame and that were not taken out of consideration, further smooth the roughness values. It is therefore advisable to use a small standard deviation multiplier and constrain the grown region to a small area.

Before determining the roughness of the grown region, a mathematical closing operation was applied to the boundary to remove any roughness introduced by inclusions, local surface tilts or image noise. The standard size of the structural element was 3 pixels. A smaller (1 pixel) and larger (5 pixels) structural element resulted in a higher and lower roughness, respectively, for all roughness values. This trend is expected, because the size of the structural element removes any roughness on the scale of the structural element or smaller. Consequently, the larger the structural element, the smoother is the boundary and the lower the roughness. A structural element of 3 pixels, which is the approximate size of the inclusions and also removes blurriness and noise on the one pixel scale, is therefore the best choice for the size of the structural element.

Finally we investigated the effect of the image scale by artificially decreasing the pixel resolution. For this, we reduced the image pixel resolution by averaging the pixel values within cells of 2×2, 4×4, 8×8 and 16×16 original pixels. We also explored the effect of decreasing the smoothing factor of the reference contour with the according image pixel resolution factor which maintains the spatial scale of the smoothing at about 2 cm. Dividing the smoothing factor by the image pixel resolution factor generally results in smaller roughness values because the smoothed reference contour approaches the shape of the rough boundary contour which naturally decreases the roughness relative to the reference contour. The only exception can be observed at a small scale roughness parameter and deduced Hapke mean slope angle at an image pixel resolution factor of 2. Here the roughness of the adjusted smoothing factor (divided by the image pixel resolution factor of 2) is larger. Nevertheless, since the values agree within their one sigma standard deviation, these values can be considered outliers.

Table 3. Approximate distance of the structures on Ryugu from the camera and the according approximate pixel resolutions in horizontal and vertical direction with reference to the image frame.

Region	Approximate distance from camera [cm]	Pixel resolution horizontal [mm]	Pixel resolution vertical [mm]
Back right	27.9	0.25	0.25
Cave	26.5	0.23	0.21
Front right	24.7	0.21	0.20
Front left	22.5	0.19	0.17
Middle	24.9	0.23	0.211

For large image pixel resolution factors (8 and 16) all roughness values decrease with decreasing image resolution (e.g. increasing image resolution factors). At these low image resolutions, the grown regions only exist of a few pixels and the boundary contour is comparatively smooth accordingly. However, when considering the adjusted smoothing of the reference contour (e.g. maintaining the spatial scale of the smoothing for the reference contour by dividing the smoothing factor of the reference contour by the image pixel resolution factor), the roughness values do not peak at the highest pixel resolutions, but at an image pixel resolution factor of 2 for the RMS-slope, hemispherical crater density, small scale roughness parameter and Hapke mean slope angle and at an image pixel resolution of 4 for the fractal dimension, Hurst exponent and JRC. This observation is probably caused by a few very bright boundary pixels (e.g. bright inclusions). Given the method of artificially reducing the image resolution by averaging the values in a given cell (e.g. 2×2 and 4×4), such pixels affect the boundary roughness on a larger scale when the image resolution is decreased. However, this roughness will not be removed by the subsequent erosion procedure as it is the case for the original image, because its structural element is on the scale of or smaller than the image resolution. Thus the effect of an increased roughness for a slightly reduced image resolution is probably an effect of the methods applied rather than a natural observation.

Following the analysis above we conclude that the following parameters are most suitable for our subsequent analysis of Ryugu's (Section 5.2) and Churyumov-Gerasimenko's (Section 5.3) small scale roughness derived from in situ images: smoothing factor of reference contour = 100, standard deviation multiplier = 1, size of structural element = 3, image pixel resolution = 1.

5.2 Ryugu roughness

Figure 5a shows the location of the five circular starting regions from which the growing algorithm was started in five different locations (structures) on Ryugu. According to their location they are labelled back right, cave, front right, left side and middle. Table 2 lists the roughness parameters for the five regions in the MasCam image of Ryugu. For all structures, the approximate pixel resolution in horizontal and vertical direction is 0.2 mm, but depending on the local topography it varies slightly (Table 3).

In addition to the roughness values derived from the MasCam image using our new method, we also extracted the roughness values using shape models from MasCam and ONC. The region on Ryugu's rock which was observed by MARA was additionally evaluated for comparison with thermally derived roughness parameters (Table 2).

The values for the RMS-slope of the five regions imaged by MasCam on Ryugu determined with the above described method is larger than the RMS-slope of the global image derived with the same

method. The values derived from the MasCam shape model is in between these two values. At the location of MARA's footprint on the Ryugu rock the RMS-slope is smallest, possibly caused by the comparatively flat local topography. The approximate roughness derived by fitting thermal measurements to the MARA night time data yields a similar value to the geometrically derived RMS-slope of this region. The shape model's RMS-slopes are generally smoother than the RMS-slope derived with our new method as they have a lower spatial resolutions compared to the image they are derived from and particularly steep slopes are averaged out. Consequently, the ONC shape model with a resolution of 20 cm has the lowest RMS-slope. The hemispherical crater density is proportional to the squared RMS-slope (Equation 3) and thus shows the same trend.

The fractal dimension, Hurst exponent and JRC also show an increased roughness with decreasing spatial resolution of the data set. The only exception to this trend is found for the small scale roughness parameter and the deduced Hapke mean slope angle. Here, the mean roughness of the five regions imaged by MasCam at a spatial resolution of 0.2 mm is slightly smaller than the roughness derived from the MasCam shape model at a spatial resolution of ~3 mm. Nevertheless, the deviation is smaller than the error of the roughness values and is thus not significant.

With the exception of the location in the front right of the MasCam image, all roughness values derived with our method have a relatively small standard deviation (Table 2). The front right part of the image is close to the bottom right corner of the image which constrained the growing region. Because the image boundary is a straight line, the roughness of a grown region reaching the image boundary is underestimated and causes the comparatively small roughness values and large errors. The fractal dimension and deduced parameters are not affected as significantly by this because the straight image boundary introduces only a small number of smooth sections which have a negligible effect on the derivation of the fractal dimension (Equation 9). Nerveless, it should be avoided to extract roughness values too close to the image boundary.

5.3 67P/Churyumov-Gerasimenko roughness

We derived the roughness parameters from the ROLIS image of Churyumov-Gerasimenko in two locations, in the centre and at the left edge of the image (Figure 5b, Table 4). As mentioned above, the image is slightly out of focus, which results in a systematic underestimation of the roughness as small scale topography will not be resolved. Thus the roughness reported on here is only a lower limit. In both locations most roughness values are similar and agree within their errors. Only the small scale roughness parameters and Hapke mean slope angles for both locations vary more significantly (Table 4). As seen by comparing the roughness parameters derived from the ONC and MasCam images, the roughness parameters derived from the global OSIRIS image of Churyumov-Gerasimenko are also generally smaller compared to the values derived from the high resolution images. It is also noticeable that due to the large image size (2048 × 2048 instead of 1024 × 1024 pixels) the errors of the roughness values derived from the OSIRIS image are comparatively small.

6 SMALL SCALE SURFACE ROUGHNESS

6.1 Influence of spatial resolution, datasets and method

Our method is sensitive to the decision made on the input parameters including the standard deviation multiplier of the circular region, the size of the structural element of the boundary contour and the smoothing factor for the reference contour. Testing the influence of these input parameters, we conclude that the best set of parameters in order to achieve comparability between different images is a standard deviation multiplier of 1, a structural element size of 3 and a reference contour smoothing factor of 100. Using these values as a base, we can achieve comparability and reproducibility for this and future data sets. However, the parameters may have to be adjusted for possible future images depending on the dataset and its quality. Varying point spread functions for different camera filters do not affect the results of the roughness values derived using our method. Image noise may influence the results on roughness with an increased noise level introducing larger roughness; however the effect is not dramatic even for high noise levels, so that our method is capable of generating comparable results for a variety of images at similar spatial resolutions.

The roughness values of Ryugu derived from the MasCam and ONC shape models and images using the newly introduced method described in Section 4 shows that the roughness is dependent on the dataset and its spatial resolution with higher spatial resolutions presenting lower roughness values. The same applies when comparing the roughness derived from the ROLIS and OSIRIS images at different spatial resolutions using our method. The spatially higher resolved images result in higher roughness. Because fractal surfaces have the characteristic that with decreased spatial resolution the total contour length decreases, it is expected that small scale roughness remains unresolved at lower resolution.

When using the same data format and looking at the same planetary body, the roughness is spatially variable. For example, using the MasCam shape model, the roughness of the entire scene is much larger than the roughness of the MARA footprint area which is a subset of the entire scene (RMS-slope: 34.9° vs 26.2°, small scale roughness parameter: 0.321 vs 0.141). The MasCam shape model shows that the MARA footprint is indeed on a relatively flat plateau surrounded by steeper slopes (Figure 2a). Even though the five regions in the MasCam image have similar distances and orientations to the camera, our image based method results in noticeably different roughness values in the five regions. The surface roughness has a significant influence on many remote sensing observations, but assuming a constant roughness value for an observation may not be advisable.

Nevertheless, considering the datasets from Ryugu and Churyumov-Gerasimenko used in this work, the roughness is higher for higher spatial resolution when considering the DTM based and our image based method separately. Generally, our image based method derives higher roughness values compared to the DTM based method which can be explained by the higher spatial resolution and the shape models' tendency to underestimate the roughness when meshing the topography. Extracting profiles from the DTMs to estimate the traditionally 2-dimensional roughness parameters, the fractal dimension, Hurst exponent and JRC, results in even lower roughness values (Tatone & Grasselli 2010). Following this observation, it is not advisable to use 3-dimensional shape models for extracting these roughness parameters as they are significantly underestimated.

Table 4. Parameters describing the roughness of comet 67P/Churyumov-Gerasimenko derived from a high resolution ROLIS image and a global OSIRIS image. The reference contour was derived by smoothing with a running mean of 100, standard deviation multiplier for region growing method set to 1 and all neighbours considered. For comparability with the Ryugu analysis, outline indentations with a size of 3 pixels across where removed from the high resolution images. The outline of the global image was not smoothed.

Location	RMS slope [°]	Hemispherical crater density	Fractal dimension	Hurst exponent	JRC	Small scale roughness parameter	Hapke mean slope angle [°]
ROLIS image centre	38.3 ± 0.6	0.61 ± 0.02	1.18 ± 0.03	0.82 ± 0.03	56.4 ± 3.4	0.346 ± 0.015	44.2 ± 1.9
ROLIS image left edge	38.1 ± 0.7	0.60 ± 0.02	1.17 ± 0.02	0.83 ± 0.02	55.1 ± 2.2	0.323 ± 0.006	41.7 ± 0.3
OSIRIS global image	34.1 ± 0.2	0.48 ± 0.01	1.11 ± 0.003	0.89 ± 0.003	45.7 ± 0.5	0.277 ± 0.004	36.5 ± 0.5

6.2 Roughness of Ryugu and 67P/Churyumov-Gerasimenko

Although the surface texture of undulating cauliflower-like features appears similar on asteroid Ryugu and comet Churyumov-Gerasimenko, the surface of Churyumov-Gerasimenko is slightly rougher compared to Ryugu on both the in situ sub-millimetre scale and the global scale. The fact that the spatial resolution of the Ryugu MasCam image is higher (0.2 mm vs ∼0.8 mm) and that the Churyumov-Gerasimenko ROLIS image is slightly out of focus implies that comet Churyumov-Gerasimenko is indeed rougher than asteroid Ryugu, because a higher spatial resolution and sharper image would result in higher resolved roughness. For example, the RMS-slope of Ryugu at a 0.8 mm spatial resolution (image pixel resolution factor of 4 in Table 1) is $36.6° ± 0.7°$, 4.6% less than the RMS-slope of $38.3° ± 0.6°$ for the same scale on Churyumov-Gerasimenko (in the image centre). The same observation can be made for the Hapke mean slope angle which is 4.7% less.

The spatial resolution of the Ryugu and Churyumov-Gerasimenko global images is similar, but all roughness parameters at this scale also indicate that Churyumov-Gerasimenko is rougher than Ryugu. The RMS-slope and Hapke mean slope angle of Ryugu at the 2 m resolution global scale are $32.9° ± 2.2°$ and $35.0° ± 5.1°$, respectively, 3.6% and 4.3% less than that of Churyumov-Gerasimenko (RMS-slope: $34.1° ± 0.2°$, Hapke mean slope angle: $36.5° ± 0.5°$). With the exception of the fractal dimension at the in situ scale, which is probably slightly distorted by the applied method as argued in Section 5.1, all roughness parameters show the same trend with Churyumov-Gerasimenko being between 2.8% and 5.5% rougher compared to Ryugu. However, given the comparatively large errors at this scale for Ryugu, the conclusion is less reliable than at smaller scales.

6.3 Roughness caused by sublimation of volatiles

Given that Ryugu is a rubble pile Cb-type asteroid (Sugita et al. 2019; Kitazato et al. 2019) and Churyumov-Gerasimenko is an active comet, differences in roughness can be expected. Laboratory experiments have shown that volatile outgassing under cometary conditions increases the near surface porosity and generates fluffy particles or aggregates from the sublimation residues that are ejected from the surface (Grün et al. 1993; Kossacki et al. 1997). The Rosetta mission at Churyumov-Gerasimenko confirmed the existence of fluffy aggregates in the size range of a 10-500 μm (Langevin et al. 2016) and 0.2-2.5 mm (Fulle et al. 2015), a scale comparable to the image resolution used in this work. It is probable that their fluffy nature is also preserved in Churyumov-Gerasimenko's near surface (Poch et al. 2016) and contribute to the observed rough texture of the comet. On the other hand, Ryugu has been reported to be neither pristine nor active and its surface materials, which were potentially compressed within the parent body and subsequently during a catastrophic impact event (Okada et al. 2020; Sugita et al. 2019), are likely

more compacted and thus may show a lower roughness compared to Churyumov-Gerasimenko.

6.4 Roughness caused by micrometeoroid impacts

Surface roughness on the centimetre and millimetre scale may also be caused by micrometeoroid impacts, as was argued for the Moon (Bastin 1966) and observed on near-Earth asteroids Itokawa and Bennu (Miyamoto et al. 2007; Ballouz et al. 2019). As described in Section 2.1, the surface of Ryugu is characterized by cauliflower-like undulations of ∼1 cm which are covered with smaller undulations of approximately 2-3 mm. The smaller undulation size is also confirmed by our measurements of the fractal dimension, in which the contour is divided into sections by the intersection of the rough and reference contour. These intersections are approximately 2.5 mm long. Furthermore, impact experiments onto carbonaceous chondrite analogue materials simulating micrometeoroid bombardment show resemblance to the observed surface morphology of Ryugu and result in a mean surface slope (32°) similar to one derived for Ryugu (Avdellidou et al. 2020).

To test if the cauliflower-like structures may be a result of spallation and compaction of micrometeoroid bombardment into a highly porous and low strength rock, we assume that a hypervelocity impact into a highly porous material can be assumed to be 10 times larger than the impactor (Tedeschi et al. 1995), thus a 250 μm particle would cause a 2.5 mm impact feature. Based on the Interplanetary Meteoroid Environment Model 2 by Soja et al. (2019), the mean impact speed of a 250 μm dust particle in a near Earth orbit is approximately 16 km/s and has an flux of $\sim 8 \cdot 10^{-9}\ m^{-2} s^{-1}$. Assuming that the rock imaged by MasCam has been exposed at the surface since Ryugu's formation (approximately 10^7 years ago (Arakawa et al. 2020)), this flux results in about $1.6 \cdot 10^5$ accumulated impacts in the imaged 25 cm × 25 cm scene or 250 impacts per cm². This implies that the total area affected by an impact of this size is approximately 10 times larger than the area of the scene meaning that the surface should show traces of such impact cater features and that micrometeoroid bombardment plays a role in the formation of Ryugu's surface roughness. However, impactors of various sizes hit the surface and specifically smaller particle impacts occur much more frequently (e.g. $\sim 5 \cdot 10^{-7}\ m^{-2} s^{-1}$ for 50 μm particles). They should erode larger crater features with time. For example, in the considered timeframe the total crater feature area of 50 μm impactors is about 30 times larger than the target area.

Further processes eroding the surface of airless bodies include solar weathering and thermal fatigue. It is possible that Ryugu's cauliflower-like texture represents an intrinsic property of the rock when exposed to multiple surface processes, including solar space weathering and thermal fatigue in addition to micrometeoroid bombardment. Given the different strength of regolith on differently classified objects and the expectation that thermal erosion of carbona-

ceous chondritic material is more efficient than thermal erosion of ordinary chondritic material (Delbo et al. 2014), the small scale surface morphology and roughness may vary between different bodies. These processes are most effective on asperities and round rock surfaces (Delbo et al. 2014; Gault et al. 1972). Given that Ryugu is a product of a catastrophic impact and has been bombarded by meteoroids since, its rocks should exhibit impact induced intrinsic fracture patterns on various scales (Tomeoka et al. 1999) encouraging thermally induced foliation along them and possibly supporting the cauliflower-like texture. In contrast, the surface of Churyumov-Gerasimenko is renewed approximately every 6.5 years when the comet passes its perihelion and ejects large amounts of its surface material. Micrometeoroid bombardment should therefore not play a significant role in the formation of surface roughness on Churyumov-Gerasimenko.

A combination of the above mentioned processes and the differences in bulk material composition and texture is likely the cause for the observation that Churyumov-Gerasimenko is rougher than Ryugu.

7 DISCUSSION

It is challenging to relate the roughness of Ryugu and Churyumov-Gerasimenko to previously derived values on other planetary bodies and materials on Earth because of the variations in applied methods, scales and data sets. Nevertheless, to achieve a sense for their roughness, we will discuss a few values of other materials and planetary bodies.

The fractal dimension and derived JRC are acknowledged parameters used in geological sciences for the estimation of the peak shear strength of a material. Common values for the fractal dimension for typical rocks (quartz, granite, sandstone, limestone, shale) range between 1.05 and 1.19 (Pal et al. 2017). The best match for Ryugu ($D = 1.16 \pm 0.04$) as well as Churyumov-Gerasimenko ($D = 1.18 \pm 0.03$) appears to be the comparatively rough limestone investigated in their survey. On larger scales, the fractal dimension has been investigated for geologic features such as lava flows on Earth ($D = 1.06 - 1.19$) as well as the Moon ($D = 1.20$) (Bruno et al. 1992). Note that all comparative values have been derived with the box counting method. The application of different methods may have an influence on the derived values (Klinkenberg 1994), but the method used in this work yields the most reliable correlation with the JRC (Li & Huang 2015).

The joint roughness coefficient relates the shear peak strength and normal stress following Equation 11. Although the assumption that Ryugu's rock is jointed due to its impact history seems reasonable, the JRC may not be an adequate parameter on Ryugu and Churyumov-Gerasimenko given the small gravitational field in which the rocks exist. The values presented in this work are guidance but do not claim that they represent the actual behaviour of rock on the small bodies.

The Hurst exponent has been derived for Eros and Itokawa, two small S-type asteroids previously visited by spacecraft, from laser ranging data. Over a range of 3 m to 1 km the global Hurst exponent of Eros was found to range between 0.81 and 0.97 (Cheng et al. 2002; Susorney & Barnouin 2018) and from scales between 8 m and 32 m the global Hurst exponent of Itokawa is 0.51 ± 0.07 (Susorney et al. 2019). The differences in roughness have been attributed to different geologic processes and internal structures of the two bodies, with Eros possessing a stronger intact interior with surface impact craters and Itokawa being a rubble pile asteroid with large variations in the geopotential and induced regolith migration as main surface

process (Susorney et al. 2019). At a scale of 2 m, we derived a similar global Hurst exponent of Ryugu of 0.92 ± 0.02 (and Churyumov-Gerasimenko (0.89 ± 0.003)) to the one derived for Eros. Although Ryugu as a rubble pile asteroid should geologically resemble Itokawa more than Eros, it is possible that the discrepancy is caused by Ryugu's comparatively symmetric shape and the different boulder size distributions at this scale. Smaller boulders seem to be buried in the regolith on Ryugu and the different composition of Ryugu and Itokawa probably results in different sized impact fragments, because S-type asteroid materials (ordinary chondrites) are stronger than C-type asteroid materials (carbonaceous chondrites) (Popova et al. 2011; Michikami et al. 2019).

The RMS-slope has been retrieved from many datasets of planetary missions applying different methods and scales. Generally, the values range between 20° and 40° for airless bodies, but variations are common with scale and location. Thermal modelling is able to retrieve roughness estimates on the scale of the thermal skin depth (centimetre scale). The best fit RMS-slope of Ryugu at the Mascot landing deduced by a thermal model site is 28.6°. Similar investigations of Ceres and the Moon result in higher RMS-slopes of 40° (Davidsson et al. 2015; Müller et al. 1999; Spencer 1990) and 30°-39° (Rozitis & Green 2011; Shkuratov et al. 2000; Spencer 1990), respectively. Radar observations of slightly higher wavelength (decimetre scale) confirm these values (Mitchell et al. 1996). The comparatively high roughness has been attributed to a fine-grained regolith covered surface that, in contrast to Ryugu (Jaumann et al. 2019), is able to form on these objects with larger gravitational pull. The roughness from thermal measurements on Churyumov-Gerasimenko has been shown to be locally highly variable and covers the range from 16° to 44° (Marshall et al. 2018). Given the high variation in published values, our estimates of the RMS-slope of Ryugu (36.6° ± 1.4°) and Churyumov-Gerasimenko (38.3° ± 0.6°) agrees with these estimates.

The RMS deviation (difference in height between points separated by a constant distance/measuring length) of planetary bodies has also been derived from shape models and laser altimeters at different resolutions (Barnouin-Jha et al. 2008; Ermakov et al. 2019). The RMS deviation directly relates to the Hurst exponent and the RMS slope can be deduced from the RMS deviation at a given measuring length (Shepard et al. 2001). Unfortunately, on the spatial scales of the data sets investigated in this work (0.2 mm to 2 m), there are no comparable data sets from any other planetary bodies to date.

Based on the stereophotogrammetric analysis of Apollo Lunar Surface Closeup Camera images, Helfenstein & Shepard (1999) were able to derive the RMS slope and Hapke roughness parameter for lunar soil on sub-millimetre scales. They found values of 16°-25° for the RMS-slope and 24°-27° for Hapke's mean slope angle of different regolith types (lunar mare, Fra Mauro regolith). Comparing these values with the stereophotogrammetrically derived shape model of Ryugu at slightly larger scales (3 mm), we find larger values of 34.9° and 26.2° (RMS-slope) for the entire rock and MARA footprint area, respectively. The Hapke mean slope angle of Ryugu for these two areas is 21.7° and 41.4°, slightly smaller and larger compared to the values derived from the Moon. Because the Moon's surface regolith is a fine grained soil covering bare rock surfaces which is not present on Ryugu, differences in roughness values are expected. This example illustrated how significantly these values can vary locally when using 3-dimensional shape models at small scales.

The Hapke mean slope angle is generally derived from photometric models and gives the roughness on a microscopic scale at which shadows influence photometric observations (Hapke 1984). In our work, the Hapke mean slope angle was derived from the small scale roughness parameter (Equation 6). Our values for the Hapke mean

slope angle are generally high (Ryugu: $40.8° \pm 3.5°$, Churyumov-Gerasimenko: $44.2° \pm 1.9°$) compared with values derived from photometric analyses of Churyumov-Gerasimenko ($19° \pm 9°$, (Ciarniello et al. 2015)) and comet Tempel 1 ($16°$-$32°$, (Li et al. 2007)). The same trend is observed for values from asteroids Eros ($24°$-$28°$, (Clark et al. 2002; Li et al. 2004)), Itokawa ($26°$-$38°$, (Kitazato et al. 2008; Tatsumi et al. 2018)) and Ceres ($18°$-$29°$ (Ciarniello et al. 2017; Li et al. 2019; Schröder et al. 2017b)). The Hapke mean slope angle of Ryugu derived from photometric fitting was found to be $28° \pm 6°$ (Tatsumi et al. 2020). The discrepancy between geometrically and photometrically derived mean slope angles has previously been explained for the Moon by Helfenstein & Shepard (1999). They suggest that below spatial resolutions of approximately 0.1 mm roughness may not be photometrically detectable. As we approach such scales in our investigation, this limitation may be applicable. Furthermore, by comparing geometrically and photometrically derived roughness values from an artificially generated terrain, Labarre et al. (2017) showed that the Hapke mean slope angle systematically underestimates the surface roughness. They attribute this behaviour to the often unsuitable assumption of a Gaussian distribution of not too large slope angles and a moderately bright material. All the latter two assumptions are not valid for the scene observed on Ryugu and Churyumov-Gerasimenko and may thus explain the significantly higher value for the Hapke mean slope angle that we derive geometrically in this work.

8 CONCLUSIONS

Based on a newly developed image analysis technique suitable to extract surface roughness, we derived a set of roughness descriptors for asteroid Ryugu and comet Churyumov-Gerasimenko based on high resolution images with 0.2 mm/pixel and ~0.8 mm/pixel covering a scene of approximately 25 cm and 80 cm horizontal extent, respectively and two global images with 2 m spatial resolution. We complemented our survey with two local shape models of Ryugu at 3 mm and 20 cm spatial resolution. The roughness descriptors include the fractal dimension and the deduced Hurst exponent and JRC, the RMS-slope and derived hemispherical crater density and the small scale self-heating parameter and deduced Hapke mean slope angle. As a Cb-type asteroid and an active comet, Ryugu's and Churyumov-Gerasimenko's composition is expected to be different. However, the general cauliflower-like texture of both bodies visible in the high resolution in situ images appears similar. The structure on Ryugu is most likely linked to erosion via micrometeoroid bombardment, solar weathering and thermal fatigue of a compacted impact rock fragment, whereas on Churyumov-Gerasimenko sublimation driven erosion of a volatile-rich regolith is potentially the most dominant process for forming surface roughness. We suggest that these different processes and compositions combined are represented by the slightly rougher descriptors (2.8% to 5.5%) for Churyumov-Gerasimenko than for Ryugu on the investigated scales.

DATA AVAILABILITY

All data derived in this work are incorporated in the article. Images from the Hayabusa2 mission will be published in the Data Archives and Transmission System (DARTS) at `https://www.darts.isas.jaxa.jp/pub/hayabusa2/onc_bundle/`. The image from the Rosetta mission is available at ESA's Planetary Science Archive (PSA) at `https://archives.esac.esa.int/psa/` and can be accessed by searching for "OSIRIS [instrument]" (Product identifier: N20140806T012001282ID30F28). The original ROLIS image is available at `ftp://psa.esac.esa.int/pub/mirror/INTERNATIONAL-ROSETTA-MISSION/ROLIS/RL-C-ROLIS-2-FSS-V1.0/DATA/` (Product identifier: ROL_FS2_141113001408_336_04) and was processed using the method described in Schröder et al. (2017a) and the polynomial coefficients provided as supplementary material to this publication. The MasCam image is available at `http://europlanet.dlr.de/Hayabusa2/MASCAM/index.html` (Product identifier: F1087378791_701_29464_r1). The digital terrain models shown in Figure 2 are available at `http://europlanet.dlr.de/Hayabusa2/MASCOT/index.html` under the according publication.

REFERENCES

Arakawa M., et al., 2020, Science, 368, 67–71
Avdellidou C., et al., 2020, Icarus, 341, 113648
Ballouz R.-L., et al., 2019, in Asteroid Science 2019. Lunar and Planetary Institute, p. 2123:1–2
Barnouin-Jha O. S., et al., 2008, Icarus, 198, 108–124
Barton N., 1976, International Journal of Rock Mechanics and Mining Sciences & Geomechanics Abstracts, 13, 255–279
Barton N., Choubey V., 1977, Rock Mechanics Felsmechanik Mécanique des Roches, 10, 1–54
Bastin J. A., 1966, Nature, 212, 171–173
Bibring J.-P., et al., 2015, Science, 349, aab0671
Bruno B. C., Taylor G. J., Rowland S. K., Lucey P. G., Self S., 1992, Geophysical Research Letters, 19, 305–308
Buhl D., Welch W. J., Rea D. G., 1968, Journal of Geophysical Research, 73, 5281–5295
Cai Y., Tang H.-m., Wang D.-j., Wen T., 2018, Mathematical Problems in Engineering, 2018, 1–14
Cheng A. F., et al., 2002, Icarus, 155, 51–74
Ciarniello M., et al., 2015, Astronomy & Astrophysics, 583, 1–14
Ciarniello M., et al., 2016, Monthly Notices of the Royal Astronomical Society, 462, S443–S458
Ciarniello M., et al., 2017, Astronomy & Astrophysics, 598, 1–14
Clark B. E., et al., 2002, Icarus, 155, 189–204
Davidsson B. J. R., Rickman H., 2014, Icarus, 243, 58–77
Davidsson B. J. R., Gutiérrez P. J., Rickman H., 2009, Icarus, 201, 335–357
Davidsson B. J. R., et al., 2015, Icarus, 252, 1–21
Davidsson B. J. R., et al., 2016, Astronomy & Astrophysics, 592, 1–30
Delbo M., et al., 2014, Nature, 508, 233–236
Ermakov A. I., Kreslavsky M. A., Scully J. E. C., Hughson K. H. G., Park R. S., 2019, Journal of Geophysical Research: Planets, 124, 14–30
Fuchs L. H., Olsen E., Jensen K. J., 1973, Smithsonian Contributions to the Earth Sciences, p. 1–39
Fulle M., et al., 2015, The Astrophysical Journal, 802, L12
Gault D. E., Hörz F., Hartung J. B., 1972, in Proceedings of the 3rd Lunar and Planetary Science Conference. The M.I.T. Press, p. 2713–2734

Gonzalez R. C., Woods R. E., 2018, Morphological Image Processing, 4th edn. Pearson, p. 694–760

Gounelle M., Zolensky M. E., 2014, Meteoritics & Planetary Science, 49, 1769–1794

Grott M., et al., 2019, Nature Astronomy, 3, 971–976

Grün E., et al., 1993, Journal of Geophysical Research: Planets, 98, 15091–15104

Hamm M., 2019, PhD thesis, Freie Universität Berlin, https://refubium.fu-berlin.de/handle/fub188/26271

Hapke B., 1981, Journal of Geophysical Research: Solid Earth, 86, 3039–3054

Hapke B., 1984, Icarus, 59, 41–59

Helfenstein P., 1988, Icarus, 73, 462–481

Helfenstein P., Shepard M. K., 1999, Icarus, 141, 107–131

Hiroi T., Peters C. M., 1991, in Proceedings of Lunar and Planetary Science. Lunar and Planetary Institute, p. 313–325

Ho T.-M., et al., 2017, Space Science Reviews, 208, 339–374

Huang S. L., Oelfke S. M., Speck R. C., 1992, International Journal of Rock Mechanics and Mining Sciences & Geomechanics Abstracts, 29, 89–98

Jaumann R., et al., 2017, Space Science Reviews, 208, 375–400

Jaumann R., et al., 2019, Science, 365, 817–820

Jiang Y., Li B., Tanabashi Y., 2006, International Journal of Rock Mechanics and Mining Sciences, 43, 837–846

Jorda L., et al., 2016, Icarus, 277, 257–278

Kameda S., et al., 2017, Space Science Reviews, 208, 17–31

Keller H. U., et al., 2007, Space Science Reviews, 128, 433–506

Keller H. U., et al., 2015, Astronomy & Astrophysics, 583, 1–16

Kitazato K., et al., 2008, Icarus, 194, 137–145

Kitazato K., et al., 2019, Science, 364, 272–275

Klinkenberg B., 1994, Mathematical Geology, 26, 23–46

Knapmeyer M., Fischer H.-H., Knollenberg J., Seidensticker K. J., Thiel K., Arnold W., Faber C., Möhlmann D., 2018, Icarus, 310, 165–193

Kossacki K. J., Kömle N. I., Leliwa-Kopystyński J., Kargl G., 1997, Icarus, 128, 127–144

Labarre S., Ferrari C., Jacquemoud S., 2017, Icarus, 290, 63–80

Lagerros J. S. V., 1996, Astronomy and Astrophysics, 310, 1011–1020

Lagerros J. S. V., 1997, Astronomy and Astrophysics, 325, 1226–1236

Lagerros J. S. V., 1998, Astronomy and Astrophysics, 332, 1123–1132

Langevin Y., et al., 2016, Icarus, 271, 76–97

Lee S. D., Lee C. I., Park Y., 1997, International Journal of Rock Mechanics and Mining Sciences, 34, 174.e1–174.e5

Li Y., Huang R., 2015, International Journal of Rock Mechanics and Mining Sciences, 75, 15–22

Li J., A'Hearn M. F., McFadden L. A., 2004, Icarus, 172, 415–431

Li J.-Y., et al., 2007, Icarus, 187, 41–55

Li J.-Y., et al., 2019, Icarus, 322, 144–167

Mandelbrot B., 1967, Science, 156, 636–638

Marshall D., et al., 2018, Astronomy & Astrophysics, 616, 1–14

Michikami T., et al., 2019, Icarus, 331, 179–191

Mitchell D. L., et al., 1996, Icarus, 124, 113–133

Miyamoto H., et al., 2007, Science, 316, 1011–1014

Morota T., et al., 2020, Science, 368, 654–659

Mottola S., Arnold G., Grothues H.-G., Jaumann R., Michaelis H., Neukum G., Bibring J.-P., 2007, Space Science Reviews, 128, 241–255

Mottola S., et al., 2015, Science, 349, aab0232.1–4

Müller T. G., Lagerros J. S. V., Burgdorf M., Lim T., Morris P. W., Salama A., Schulz B., Vandenbussche B., 1999, in Cox P., Kessler M., eds, ESA Special Publication Vol. 427, The Universe as Seen by ISO. ESA Special Publication, p. 141–144

Odling N. E., 1994, Rock Mechanics and Rock Engineering, 27, 135–153

Okada T., et al., 2020, Nature, 579, 518–522

Pal S. K., Rao K. U. M., Kumar P. S., Rajasekar R., 2017, Archives of Metallurgy and Materials, 62, 1787–1793

Poch O., Pommerol A., Jost B., Carrasco N., Szopa C., Thomas N., 2016, Icarus, 267, 154–173

Popova O., Borovička J., Hartmann W. K., Spurný P., Gnos E., Nemtchinov I., Trigo-Rodríguez J. M., 2011, Meteoritics & Planetary Science, 46, 1525–1550

Poulet F., et al., 2016, Monthly Notices of the Royal Astronomical Society, 462, S23–S32

Preusker F., et al., 2015, Astronomy & Astrophysics, 583, A33

Preusker F., et al., 2019, Astronomy & Astrophysics, 632, 1–6

Reeves M. J., 1985, International Journal of Rock Mechanics and Mining Sciences & Geomechanics Abstracts, 22, 429–442

Rost E., Hecker C., Schodlok M. C., Van der Meer F. D., 2018, Minerals, 8, 1–21

Rozitis B., Green S. F., 2011, Monthly Notices of the Royal Astronomical Society, 415, 2042–2062

Rozitis B., Green S. F., 2012, Monthly Notices of the Royal Astronomical Society, 423, 367–388

Rozitis B., Green S. F., 2013, Monthly Notices of the Royal Astronomical Society, 433, 603–621

Scholten F., et al., 2019, Astronomy & Astrophysics, 632, 1–6

Schröder S. E., et al., 2017a, Icarus, 285, 263–274

Schröder S. E., et al., 2017b, Icarus, 288, 201–225

Schröder S. E., et al., 2020, Planetary Science Journal, submitted, 30

Shepard M. K., Campbell B. A., 1998, Icarus, 134, 279–291

Shepard M. K., Campbell B. A., Bulmer M. H., Farr T. G., Gaddis L. R., Plaut J. J., 2001, Journal of Geophysical Research: Planets, 106, 32777–32795

Shkuratov Y., Stankevich D., Sitko M. L., Sprague L. A., 2000, in Sitko M. L., Sprague A. L., Lynch D. K., eds, Astronomical Society of the Pacific Conference Series Vol. 196, Thermal Emission Spectroscopy and Analysis of Dust, Disks, and Regoliths. Astronomical Society of the Pacific, p. 211–230

Soja R. H., et al., 2019, Astronomy & Astrophysics, 628, 1–13

Spencer J. R., 1990, Icarus, 83, 27–38

Spohn T., et al., 2015, Science, 349, aab0464.1–4

Steinbrügge G., Stark A., Hussmann H., Wickhusen K., Oberst J., 2018, Planetary and Space Science, 159, 84–92

Steinbrügge G., et al., 2020, Icarus, 343, 113669

Sugita S., et al., 2019, Science, 364, 1–11

Susorney H. C. M., Barnouin O. S., 2018, Icarus, 314, 299–310

Susorney H. C. M., Johnson C. L., Barnouin O. S., Daly M. G., Seabrook J. A., Bierhaus E. B., Lauretta D. S., 2019, Icarus, 325, 141–152

Tatone B. S. A., Grasselli G., 2009, Review of Scientific Instruments, 80, 125110.1–10

Tatone B. S. A., Grasselli G., 2010, International Journal of Rock Mechanics and Mining Sciences, 47, 1391–1400

Tatsumi E., et al., 2018, Icarus, 311, 175–196

Tatsumi E., et al., 2020, Astronomy & Astrophysics, 639, 1–19

Tedeschi W. J., Remo J. L., Schulze J. F., Young R. P., 1995, International Journal of Impact Engineering, 17, 837–848

Tomeoka K., Yamahana Y., Sekine T., 1999, Geochimica et Cosmochimica Acta, 63, 3683–3703

Tse R., Cruden D. M., 1979, International Journal of Rock Mechanics and Mining Sciences & Geomechanics Abstracts, 16, 303–307

Ulamec S., et al., 2016, Acta Astronautica, 125, 80–91

Watanabe S.-i., Tsuda Y., Yoshikawa M., Tanaka S., Saiki T., Nakazawa S., 2017, Space Science Reviews, 208, 3–16

Watanabe S., et al., 2019, Science, 364, 268–272

Xie H.-P., Pariseau W. G., 1994, Science in China (Series B), 37, 1516–1524

Xu Y. F., Sun D. A., 2005, Géotechnique, 55, 691–695

Yano H., et al., 2006, Science, 312, 1350–1353

Zahouani H., Vargiolu R., Loubet J. L., 1998, Mathematical and Computer Modelling, 28, 517–534

This paper has been typeset from a TEX/LATEX file prepared by the author.